APPLIED SCIENCES AND ENGINEERING

Transparent and conductive nanomembranes with orthogonal silver nanowire arrays for skin-attachable loudspeakers and microphones

Saewon Kang*, Seungse Cho*, Ravi Shanker, Hochan Lee, Jonghwa Park, Doo-Seung Um, Youngoh Lee, Hyunhyub Ko†

We demonstrate ultrathin, transparent, and conductive hybrid nanomembranes (NMs) with nanoscale thickness, consisting of an orthogonal silver nanowire array embedded in a polymer matrix. Hybrid NMs significantly enhance the electrical and mechanical properties of ultrathin polymer NMs, which can be intimately attached to human skin. As a proof of concept, we present a skin-attachable NM loudspeaker, which exhibits a significant enhancement in thermoacoustic capabilities without any significant heat loss from the substrate. We also present a wearable transparent NM microphone combined with a micropyramid-patterned polydimethylsiloxane film, which provides excellent acoustic sensing capabilities based on a triboelectric voltage signal. Furthermore, the NM microphone can be used to provide a user interface for a personal voice-based security system in that it can accurately recognize a user's voice. This study addressed the NM-based conformal electronics required for acoustic device platforms, which could be further expanded for application to conformal wearable sensors and health care devices.

INTRODUCTION

Recently, various electronic devices have been developed to mimic the comprehensive capabilities of the human senses for a wide range of potential applications, such as electronic skin (E-skin) for tactile sensing (*1*–*3*), artificial basilar membranes for hearing (*4*, *5*), and an artificial throat for speaking (*6*). The human voice has been an important biosignal for realizing user interfaces with the rapid growth of the "Internet of Things (IoT)," interconnecting humans and machines. In addition, acoustic hearing and speaking devices have attracted great attention as essential technologies for many potential human-machine interactive applications, such as voice security, the control of drones and robots, communication with artificial intelligence (AI), and many kinds of voice recognition system (*7*, *8*). For these applications, personal wearable acoustic devices require advanced flexible, portable, and miniaturized appliances capable of detecting or producing the human voice, as well as sounds (*6*, *9*–*14*). Previously, Fan *et al.* (*10*) demonstrated an ultrathin, self-powered, and paper-like microphone for recording the human voice. This microphone generated a triboelectric voltage in response to sound pressure (*10*). In addition, Tao *et al.* (*6*) developed a graphene-based artificial throat that can function as both loudspeaker and microphone. Despite the high levels of performance and functionality available from these flexible acoustic devices, they remain rigid, which prevents their intimate integration with the human skin or other electronic devices intended for a wearable device platform. Furthermore, wearable electronics are nowadays required to be ultrathin, lightweight, and transparent to offer better convenience and appearance (*15*), which may yield emerging technologies, such as imperceptible electronics, skin-attachable E-skin, and conformal electronics (*16*–*23*). On the basis of these concepts, highly conformal device/skin contact has become an essential feature because these devices can be directly attached to an uneven surface or even human skin, which can be characterized as a curvilinear and nonflat surface with a complex topology (*24*). To achieve conformal device/skin contact, researchers have suggested various approaches, including decreasing the substrate thickness, using bioinspired structures, and adopting a microhair architecture, thus enabling the realization of a conformal interaction with the skin (*22*, *24*, *25*).

Freestanding nanomembranes (NMs) with a nanoscale thickness of less than a few hundred nanometers can provide a powerful platform for conformal electronics that offers many features such as lightness, excellent flexibility, optical transparency, and conformability (*26*, *27*), which are not available with bulk materials. Graphene-based conformal devices formed on ultrathin polymer NM substrates have been developed for skin-attachable devices (*22*). In addition, conformal tactile sensors fabricated by forming MoS_2 semiconductors on NM substrates have demonstrated good optical transparency and mechanical flexibility for high-sensitivity E-skin applications (*21*). Although these NM-based electronics are characterized by an extremely low bending stiffness, making them capable of achieving conformal contact with an uneven surface, the mechanical properties of these polymeric NMs are still limited by their low fracture toughness, which can result in mechanical failures, such as cracks or voids caused by the application of an externally applied strain.

Hybrid NMs differ from polymeric NMs in that the electrical, optical, and mechanical properties of the NMs are determined by the type of the loading material, which can be metal nanoparticles (NPs), metal nanowires (NWs), carbon nanotubes (CNTs), or graphene (*26*, *28*–*30*). In this respect, silver NW (AgNW)/polymer composite NMs are attractive candidates because they have excellent mechanical and electrical properties due to the large aspect ratio of the AgNWs used as reinforcement (*28*, *31*). In addition, AgNW networks can be easily prepared by cost-effective and large-scale solution-based processes, such as spin coating, drop casting, rod coating, and spray coating (*32*–*36*). A few studies have addressed the mechanical properties of freestanding AgNW/polymer composite NMs formed using a layer-by-layer assembly technique (*28*, *37*). Gunawidjaja *et al.* (*37*) investigated the mechanical properties of unidirectionally oriented AgNW

School of Energy and Chemical Engineering, Ulsan National Institute of Science and Technology, Ulsan Metropolitan City 689-798, Republic of Korea.
*These authors contributed equally to this work.
†Corresponding author. Email: hyunhko@unist.ac.kr

embedded in polymeric NMs, which results in a significant enhancement of the mechanical strength along the NW orientation. However, the scalability and fabrication process are not suitable for commercial applications. Furthermore, to the best of our knowledge, there have been no attempts to exploit hybrid NMs with an AgNW network to fabricate NM-based wearable electronic devices.

Here, we introduce ultrathin, conductive, and transparent hybrid NMs that can be applied to the fabrication of skin-attachable NM loudspeakers and microphones, which would be unobtrusive in appearance because of their excellent transparency and conformal contact capability. Our hybrid NMs consist of an orthogonal AgNW array embedded in a polymer matrix, which substantially enhances the electrical and mechanical properties of ultrathin polymer NMs without any significant loss in the optical transparency due to the orthogonal array structure.

RESULTS

Ultrathin, transparent, and conductive hybrid NMs

Figure 1A is a schematic of the fabrication procedure for transparent and conductive hybrid NMs using orthogonal AgNW arrays as the nanoreinforcement, as well as a polymer matrix. Zinc oxide (ZnO) films (thickness, ~200 nm) deposited on silicon (Si) substrates are prepared as a sacrificial layer to allow NMs to be released from the Si substrate after the fabrication process. We chose ZnO films to ensure the alignment of the AgNW arrays, in that the sacrificial films would not dissolve in either deionized (DI) water or ethanol. The orthogonal AgNW arrays were fabricated onto the ZnO layer by using a solution-based bar-coating assembly technique (*38*). Subsequently, parylene-C films were deposited onto the orthogonal AgNW arrays by a chemical vapor deposition (CVD) method to form a polymer matrix of nanometer thickness. We chose this material because of its good biocompatibility and chemical stability (*39*). The as-fabricated hybrid NMs on Si substrates were placed in an etchant solution [citric acid 10 weight % (wt %) dispersed in DI water] to dissolve the ZnO layer and release the hybrid NMs. Figure 1B shows a hybrid NM suspended on the surface of the etchant solution. A suspended hybrid NM can be easily transferred without any damage by using an anodic aluminum oxide (AAO) template as a carrier, due to their low friction originating from the nanoporous surface structure (fig. S1). Figure 1C shows dark-field optical micrographs of an orthogonal AgNW array produced by the bar-coating process. The fast Fourier transform (FFT) image in the inset clearly shows the cross-configuration of the geometry. The orthogonal AgNW arrays are tightly embedded in the polymer matrix, giving a total thickness of 100 nm, as shown in both the cross-sectional scanning electron microscopy (SEM) and atomic force microscopy images (Fig. 1D and fig. S2).

We determined the optical and electrical properties of the hybrid NMs from the density of the orthogonal AgNW array produced via a multistep assembly process in which the density of orthogonal AgNW

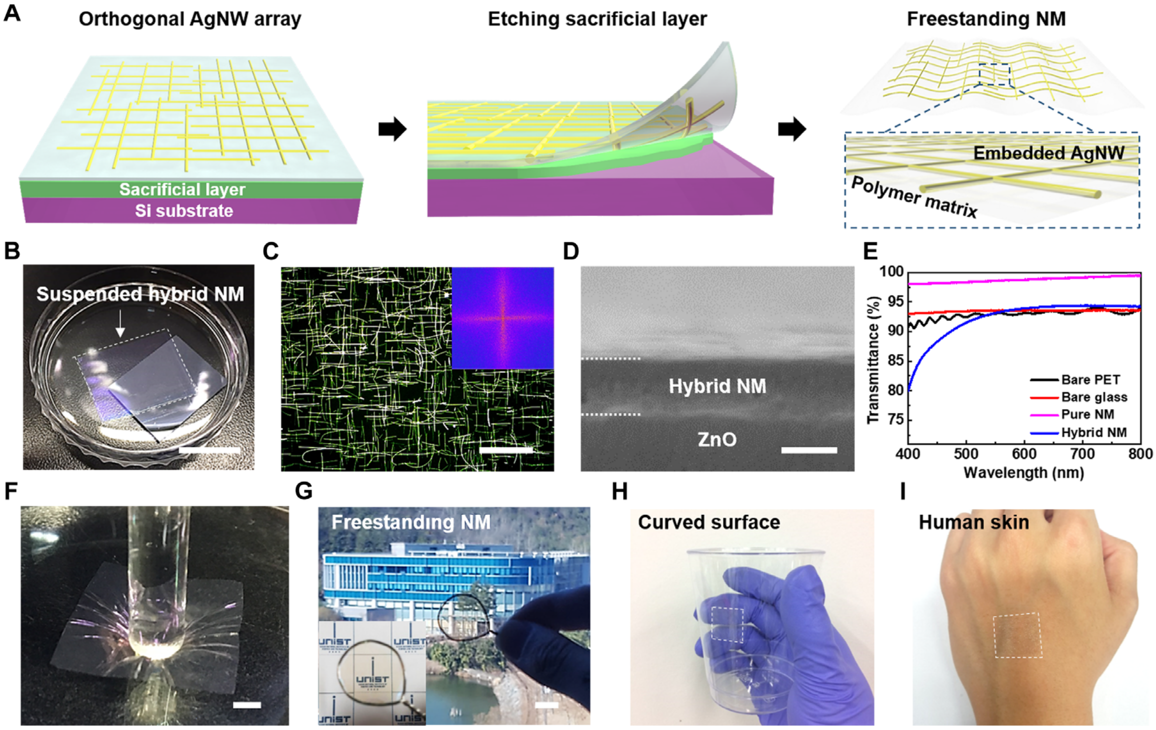

Fig. 1. Fabrication of freestanding hybrid NMs with orthogonal AgNW arrays. (**A**) Schematic of fabrication procedure for freestanding hybrid NMs with orthogonal AgNW arrays embedded in a polymer matrix. (**B**) Freestanding AgNW composite NMs floating on a surface of water. Scale bar, 1 cm. (**C**) Dark-field optical microscope image of orthogonal AgNW arrays. The inset shows an FFT image of the optical micrograph, corresponding to its surface geometric structure. Scale bar, 40 μm. (**D**) Cross-sectional SEM image of an as-fabricated hybrid NM on a ZnO/Si substrate. Scale bar, 100 nm. (**E**) Optical transmittance of polymer NMs, hybrid NMs, bare PET, and bare glass in the visible range of 400 to 800 nm. The air is used as a reference. (**F**) Photograph of a hybrid NM on the surface of water under compressive force applied by a glass rod. Scale bar, 3 mm. (**G**) A freestanding hybrid NM supported by a wire loop. Inset shows the high transparency of the hybrid NM. Scale bar, 1 cm. (**H**) Hybrid NMs transferred onto curvilinear surface and (**I**) onto human skin.

arrays was controlled by varying the number of coatings (fig. S3) (*38*). For a three-step coating, the pure orthogonal AgNW array has a high transmittance of 97.4% at a wavelength of 550 nm and a low sheet resistance of 47.4 ohm/sq (fig. S3). The pure polymer NM exhibits a high transmittance of 98.2% at the same wavelength. In particular, the hybrid NMs composed of orthogonal AgNW arrays embedded in the polymer matrix exhibit an excellent transmittance of 93.1% at a wavelength of 550 nm without any significant optical loss, which is comparable to transmittances of other conventional transparent substrates such as polyethylene terephthalate (PET; 92.9%) and glass (93.5%; Fig. 1E). Our hybrid NMs differ from other types of hybrid NMs integrated with nanomaterials, such as NPs, NWs, CNTs, and graphene (*26*, *28*–*30*), in that the orthogonal AgNW arrays provide not only excellent electrical conductivity and optical transparency but also a significant improvement to the overall mechanical properties of the polymer matrix due to the effective interfacial interaction between the AgNW and the polymer matrix, resulting in efficient load transfer within the polymer matrix (*40*, *41*). Consequently, hybrid NMs suspended on the water surface maintain their original shape without any damage, such as cracking or fracturing when struck with a glass rod or when lifted and lowered with a plastic pipette (Fig. 1F and movie S1). Furthermore, our transparent and freestanding hybrid NMs can be transferred to any three-dimensional (3D) surface with a curvilinear and complex morphology due to the low film thickness, which makes the hybrid NMs unobtrusive (Fig. 1, G to I). Note that hybrid NMs, placed on the back of a person's hand, maintain their electrical conductivity without breaking when subjected to compression or stretching (movie S2).

Conformal contact capabilities of skin-attachable hybrid NMs

To quantitatively evaluate the conformal contact capabilities of hybrid NMs, we calculated their bending stiffness (*EI*), as described in fig. S4 and section S1. As a result, the hybrid NMs were found to have a bending stiffness of 5.51 GPa·μm^4, which is comparable with previously reported values (*20*, *22*, *42*). Therefore, our hybrid NMs offer a high degree of bendability with a small bending radius of ~2.2 μm due to their low bending stiffness caused by their nanoscale thickness, which facilitates intimate contact, even with 3D surfaces (fig. S5). Figure 2A is a schematic of the conformal contact properties of a hybrid NM attached to human skin, the epidermis of which has a curvilinear and uneven surface with a complex topography. To prove the conformal contact capability of our NMs, we transferred hybrid NMs to the epidermis of human skin by using an AAO template as a carrier. Figure 2B shows a hybrid NM after being transferred to a human finger, conformably contacting the fine ridges of the fingertip, the surface roughness of which is a few hundred micrometers. To further investigate the

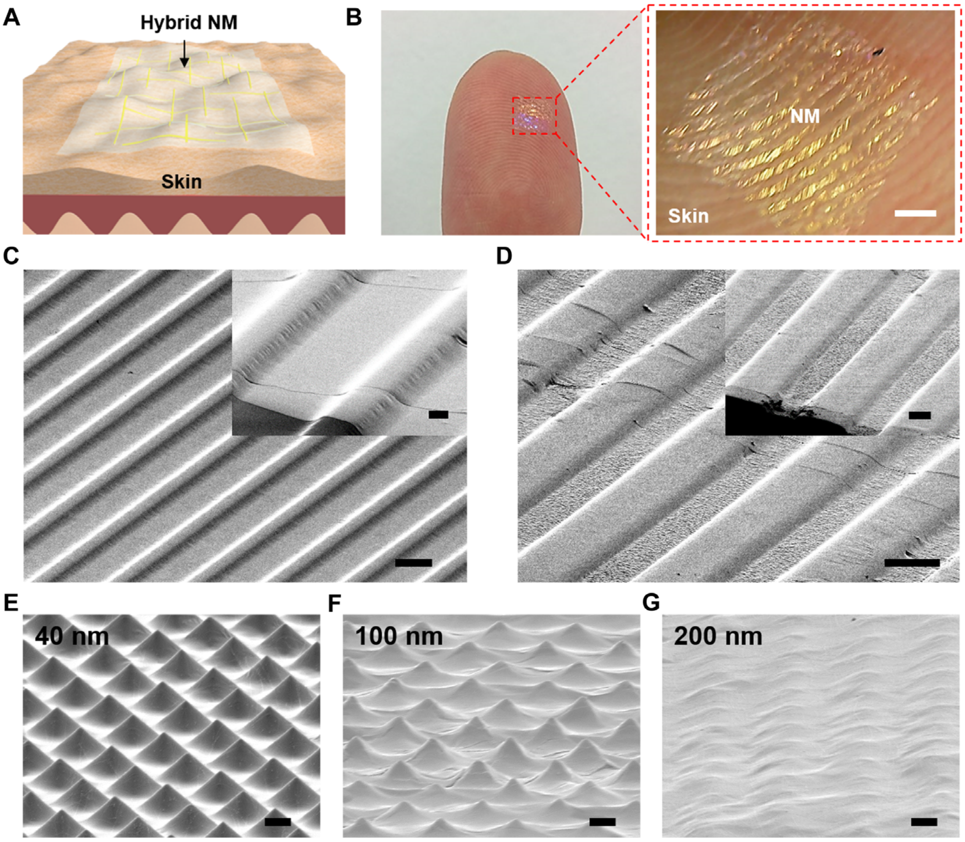

Fig. 2. Conformal contact of AgNW composite hybrid NMs on 3D microstructures. (**A**) Schematic of conformal contact of NMs on the skin surface. (**B**) Hybrid NMs attached to a thumb. The inset shows a micrograph of a hybrid NM on the skin of a fingertip. Scale bar, 1 mm. (**C** and **D**) SEM images of the hybrid NMs transferred on line-patterned 3D PDMS microstructures with a line width of 20 μm (C) and 120 μm (D). Scale bars, 50 and 100 μm, respectively. The insets show magnified images with scale bars indicating 10 μm (C) and 50 μm (D). SEM images of hybrid NMs with thicknesses of 40 nm (**E**), 100 nm (**F**), and 200 nm (**G**) transferred onto micropyramid-patterned 3D PDMS microstructures with a diameter of 10 μm and a height of 7 μm. Scale bars, 5 μm.

conformal bendability, we transferred the hybrid NMs to polydimethylsiloxane (PDMS) that had been patterned with lines with a width of 20 and 120 μm. The transferred hybrid NMs closely adhered to the line-patterned PDMS surface, even along the edges of the line patterns, implying that the hybrid NMs have excellent bendability (Fig. 2, C and D, and fig. S6). To show the conformal contact on a 3D surface, we transferred hybrid NMs with different film thicknesses (40, 100, and 200 nm) onto micropyramid-patterned PDMS substrates (diameter, ~10 μm; height, ~7 μm; Fig. 2, E to G). The results showed that, 40- and 100-nm-thick hybrid NMs can form a conformal contact on the surface of micropyramid-patterned PDMS with the step surface coverage (ratio of film-covered height to the total height of the 3D structure) of ~92 and ~73%, while 200-nm-thick hybrid NMs cannot conformably cover the surface with the lowest step surface coverage of ~15% (fig. S7).

Mechanical properties of hybrid NMs

In general, conventional hybrid NMs containing nanomaterials exhibit enhanced mechanical properties relative to pure polymer NMs due to the reinforcing effect of the fillers in the nanocomposite (*28*). To evaluate the mechanical properties of hybrid NMs, we performed a mechanical test to measure the Young's modulus (E), as obtained from the wrinkles formed by the capillary force generated by placing a droplet of water in the center of a floating NM, using an optical microscope (Fig. 3A) (*43*). We observed that the number of wrinkles (N), as induced by the surface tension of the water droplet, decreased as the density of the orthogonal AgNW array increased (fig. S8). Hybrid NMs generate fewer wrinkles ($N < 39$) than pure polymer NMs ($N > 49$) without AgNWs. To further investigate the effect of an orthogonal AgNW array loading material on the Young's modulus, we plotted the number of wrinkles in the NM as a function of the combined

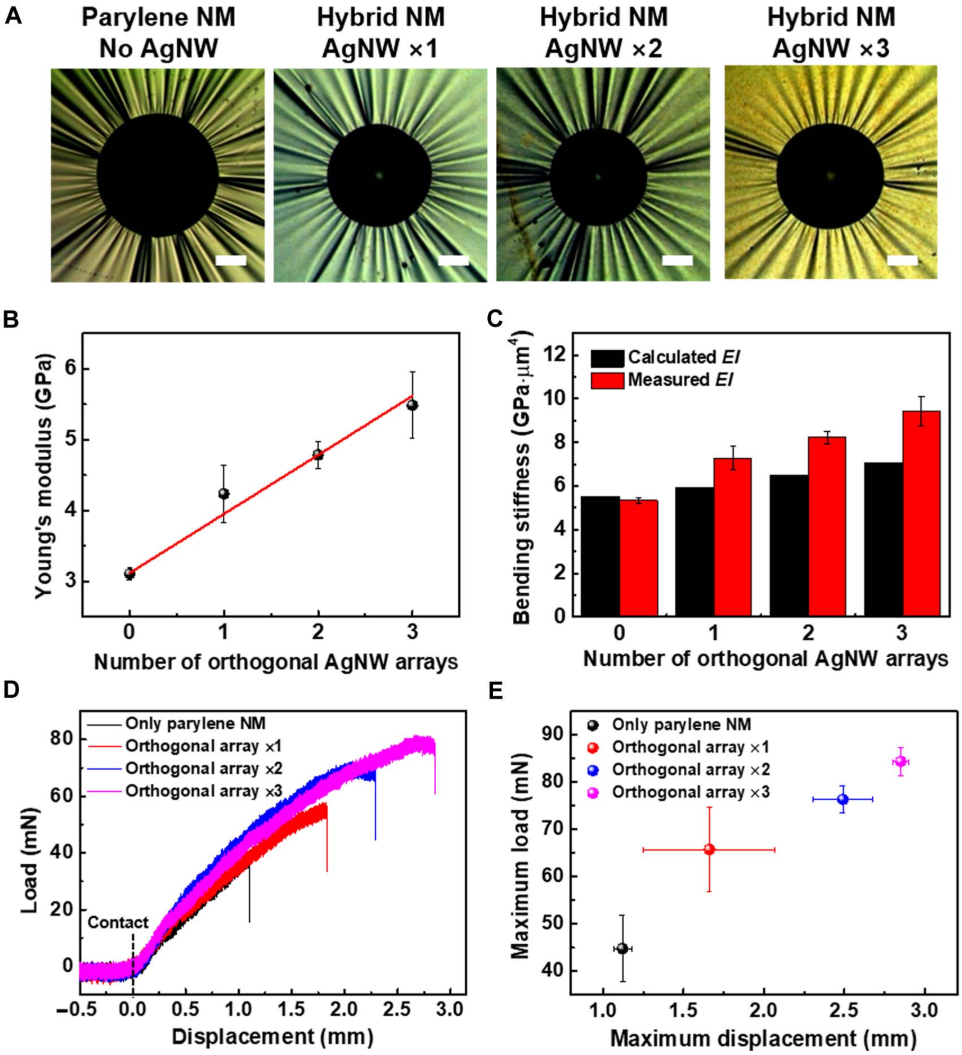

Fig. 3. Mechanical properties of hybrid NMs with orthogonal AgNW arrays. (**A**) Freestanding hybrid NMs with different densities of orthogonal AgNW arrays floating on the water surface. NMs are wrinkled by a water droplet of radius ≈ 0.3 mm. The number of wrinkles decreases as the density of the AgNWs increases. Scale bars, 200 μm. (**B**) Young's modulus (E) of NMs as calculated from the wrinkle tests. (**C**) Comparison of calculated and experimental bending stiffness of hybrid NMs with orthogonal AgNW arrays of different densities. We calculated the measured bending stiffness using the Young's modulus that had been experimentally obtained with the capillary wrinkling method. (**D**) Applied indentation load versus displacement of freestanding hybrid NMs as a function of the density of orthogonal AgNW arrays. (**E**) Maximum indentation load versus displacement of hybrid NMs as a function of orthogonal AgNW arrays.

dependence on the radius of the water droplet (a) and the thickness of the NM (h), captured by scaling $N \sim a^{1/2}h^{-3/4}$, as shown in fig. S9. Thus, the Young's modulus of the hybrid NMs was calculated using Eq. 1 (*43*)

$$N = C_N \left[\frac{12(1-\Lambda^2)\gamma}{E}\right]^{1/4} a^{1/2}h^{-3/4} \tag{1}$$

where C_N is the numerical constant, Λ is the Poisson ratio, and γ is the surface tension of the droplet. We obtained $C_N = 3.2$ from the experimental results, with the slope of the fit line shown in fig. S9. The Young's modulus of the hybrid NMs increases linearly with an increase in the density of the orthogonal AgNW arrays (Fig. 3B). We also acquired the bending stiffness of the hybrid NMs from the experimentally measured Young's modulus, as shown in Fig. 3B. We compared the calculated and measured bending stiffness of the hybrid NMs, as shown in Fig. 3C (detailed information on the calculated and measured bending stiffnesses is given in sections S1 and S2). The measured bending stiffness (5.18 to 9.62 GPa·μm^4) increases with the density of the orthogonal AgNW arrays, which is similar to the tendency of the calculated bending stiffness (5.33 to 6.88 GPa·μm^4). The slight difference in the calculated and measured values can be attributed to the presence of random NW-NW junctions, which were not considered in the bending stiffness calculation shown in fig. S4.

We also performed an indentation test to measure the mechanical strength and ductility of the hybrid NMs while varying the density of the orthogonal AgNW array. In this test, freestanding hybrid NMs, placed over a hole in the supporting plate, were deformed by the application of a compressive force and then fractured when the force exceeded the maximum load that could be applied to the NMs (fig. S10). Figure 3D shows typical force versus indentation displacement (*F-d*) curves obtained by increasing the density of the orthogonal NW arrays. The *F-d* curves shown in Fig. 3D clearly show the increase in the tensile strength of the parylene as the density of the stiff NW array increases. Generally, adding NPs increases the stiffness and strength of a composite film. On the other hand, this reduces the ductility of the composite film. In contrast to this behavior, our hybrid NM exhibits a progressive increase in the indentation displacement as the AgNW density increases, owing to the high ductility of nanosized AgNWs with the large aspect ratio and stretchability of the AgNW networks, which is advantageous for flexible device applications (*44*, *45*).

Figure S11 shows the complete loading and unloading curves for polymer NMs and hybrid NMs. For the cyclic test, we repeatedly applied a predefined indentation load to the NMs at a loading/unloading rate of 0.1 mm/s. For an indentation load of ~27 mN, the *F-d* curves exhibit hysteresis behaviors for both the hybrid and polymer NMs, indicating the inelastic deformation of the AgNW networks and parylene polymer chains in the NMs during the indentation. The larger hysteresis of the hybrid NMs than the polymer NMs can be attributed to the larger inelastic deformation of the hybrid NMs, in which the breakdown of the interfacial bonding between the AgNW and the polymer matrix causes a larger energy dissipation than those caused by the polymer chain rearrangement (*46*, *47*). During the repeated loading-unloading cycles, the hysteresis gradually decreases. In particular, the hysteresis of the hybrid NMs was greatly suppressed because of the permanent failure of the AgNW and polymer interface. At a lower indentation load (~11 mN), both the hybrid and polymer NMs exhibit weak hysteresis behaviors due to the elastic deformations. The maximum load and displacement that can be applied to the hybrid NMs until their failure gradually increase with the density of the orthogonal AgNW array (Fig. 3E). The maximum load and displacement of the hybrid NMs with orthogonal AgNW arrays (load, 84.3 ± 3.03 mN; displacement, 2.85 ± 0.05 mm) are much higher than those of the pure polymer NMs (load, 44.8 ± 7.05 mN; displacement, 1.12 ± 0.06 mm). This could be attributed to the efficient load transfer between the orthogonal AgNW array and the polymer matrix in a nanocomposite system (*40*). These results suggest that the orthogonal AgNW array is an excellent loading material for enhancing the overall mechanical properties of a hybrid NM system.

Skin-attachable and transparent NM loudspeaker

For a proof-of-concept demonstration, we fabricated a skin-attachable loudspeaker using hybrid NMs. The speaker can emit thermoacoustic sound by the temperature-induced oscillation of the surrounding air. Here, the temperature oscillation is caused by Joule heating of the orthogonal AgNW array upon the application of an AC voltage. Figure 4A is a schematic of the skin-attachable NM loudspeaker emitting thermoacoustic sound, where periodic Joule heating generates a temperature oscillation, which then propagates into the surrounding medium, causing an air pressure oscillation (that is, a sound wave). An infrared (IR) image of the loudspeaker with an orthogonal AgNW array reveals a highly uniform Joule heating performance with a slight increase in the surface temperature during a flow of AC 10 V at 10 kHz (fig. S12). Figure 4B shows the acoustic measurement system used to analyze the sound, as emitted from the NM loudspeaker upon the application of a voltage with a sinusoidal waveform, produced by a function generator. We used a commercial microphone to collect and record the sound produced by the loudspeaker. To characterize the sound generation of the loudspeaker, we confirmed that the sound pressure level (SPL) of the output sound increases linearly as the distance between the microphone and the loudspeaker decreases (fig. S13).

Figure 4C shows the sound pressure produced by loudspeakers based on a hybrid NM and a thick PET film (with a PET thickness of around 220 μm) with an orthogonal AgNW array, as a function of the input power at a frequency of 10 kHz and a fixed measurement distance of 3 cm. The output sound pressure from both loudspeakers increases linearly as the input power is increased. Notably, the loudspeaker based on a hybrid NM produces a much larger sound pressure than the one that uses a thick PET film with an orthogonal AgNW array at the same input power. Figure 4D shows the SPL spectrum as the sound frequency is varied over a range of 1 to 20 kHz. We confirmed that the SPL of both the thick-film and NM loudspeakers gradually increases with the sound frequency. These results can be explained by the following theoretical formula (*48*)

$$P_{\mathrm{rms}} = \frac{\sqrt{\alpha}\rho_0}{2\sqrt{\pi}T_0} \cdot \frac{1}{r} \cdot P_{\mathrm{input}} \cdot \frac{\sqrt{f}}{C_s} \tag{2}$$

where P_{rms} is the root-mean-square sound pressure, α is the thermal diffusivity of the ambient gas, ρ_0 is the density, T_0 is the temperature, r is the distance between the loudspeaker and the microphone, P_{input} is the input power, f is the sound frequency, and C_s is the heat capacity per unit area. Our experimental results are well matched with the theoretical prediction given by Eq. 2, where the generated sound pressure increases as a function of the input power and sound frequency. Notably, NM loudspeakers produce a massive enhancement in the SPL across the entire measured frequency range compared to thick-film loudspeakers, which we attribute to a reduction in the heat loss caused by the substrates (*49*, *50*). In general, a lower thermal effusivity of the substrate is preferred to facilitate the effective exchange of thermal energy with the surrounding air to efficiently generate sound (*50*). The thermal effusivity (e) can be calculated using the equation $e = (\kappa \cdot \rho \cdot C_p)^{1/2}$, where κ is the thermal conductivity, ρ is the density, and C_p is the heat capacity. We obtained $e = 262\ \text{W} \cdot \text{s}^{1/2}/\text{m}^2 \cdot \text{K}$ for the parylene NMs using literature values of $\kappa = 0.08$ W/mK, $\rho = 1230\ \text{kg/m}^3$, and $C_p = 700$ J/kg·K, which are relatively small values compared to other materials (*49*). In NM loudspeakers, however, the low film thickness is more crucial to the minimization of the heat dissipation necessary for the enhanced sound pressure than the thermal effusivity (*50*). To further validate the effect of heat loss when the NM is relatively thin, we calculated the theoretical SPL for both a thick PET film and a hybrid NM loudspeaker as a function of the frequency, using Eq. 3 (*50*)

$$\Delta P = \frac{3}{4\pi}\frac{P_{\text{input}} f}{v_{\text{air}}^2\, r}\frac{e_{\text{air}}}{2e_{\text{air}} + (d_{\text{sub}}\rho_{\text{sub}}C_{\text{p,sub}} + d_{\text{film}}\rho_{\text{film}}C_{\text{p,film}})\sqrt{2\pi f}} \qquad (3)$$

where ΔP is the sound pressure, v_{air} is the speed of sound in air, e_{air} is the thermal effusivity of air, ρ_{sub} and ρ_{film} are the density of the substrate and film, $C_{\text{p,sub}}$ and $C_{\text{p,film}}$ are the heat capacity of the substrate and film, and d_{sub} and d_{film} are the thickness of the substrate and film, respectively. We obtained the SPL for both loudspeakers by converting the sound pressure to SPL. As a result, the change in the theoretical SPL as a function of the frequency for both loudspeakers exhibited agreement with our experimental results (Fig. 4D). Note that the huge enhancement of the SPL is not mainly attributed to the discrepancy in the thermal effusivity of the parylene NMs and PET films. The theoretical calculation of SPL reveals that the influence of thermal effusivity on the SPL is negligible for films with a nanoscale thickness, while the low thermal effusivity enhances the SPL in the case of a thick-film loudspeaker system (fig. S14). Therefore, the considerable enhancement in the SPL of the NM loudspeaker could be attributed to the efficient heat transfer to the surroundings resulting from the reduction in the heat loss to the very thin substrate (*49*). To demonstrate wearable and skin-attachable applications, we mounted the NM loudspeaker to the back of a subject's hand and connected it by two copper wire electrodes. This loudspeaker is unobtrusive in appearance due to the high transmittance and intimate contact with the human skin (Fig. 4E). We were able to play and recognize Paganini's well-known *La Campanella* violin concerto when played through the NM loudspeaker attached to the skin (movie S3).

Wearable and transparent NM microphone

To further demonstrate the applicability of hybrid NMs, we designed a wearable and transparent microphone using hybrid NMs combined with micropatterned PDMS (NM microphone). The resulting device was able to detect sound and recognize a human voice. Figure 5A illustrates the structure of the skin-attachable NM microphone, consisting of a hybrid NM mounted to a holey PDMS film and micropyramid-patterned PDMS film. This sandwich-like structure can precisely detect the sound and vibration of the vocal cords by the generation of a triboelectric voltage resulting from the coupling effect of the contact electrification and electrostatic induction (*51*). Figure 5B shows the NM microphone, which is highly transparent. We used the holey PDMS film to receive a sound wave and to support freestanding NMs. We selected a

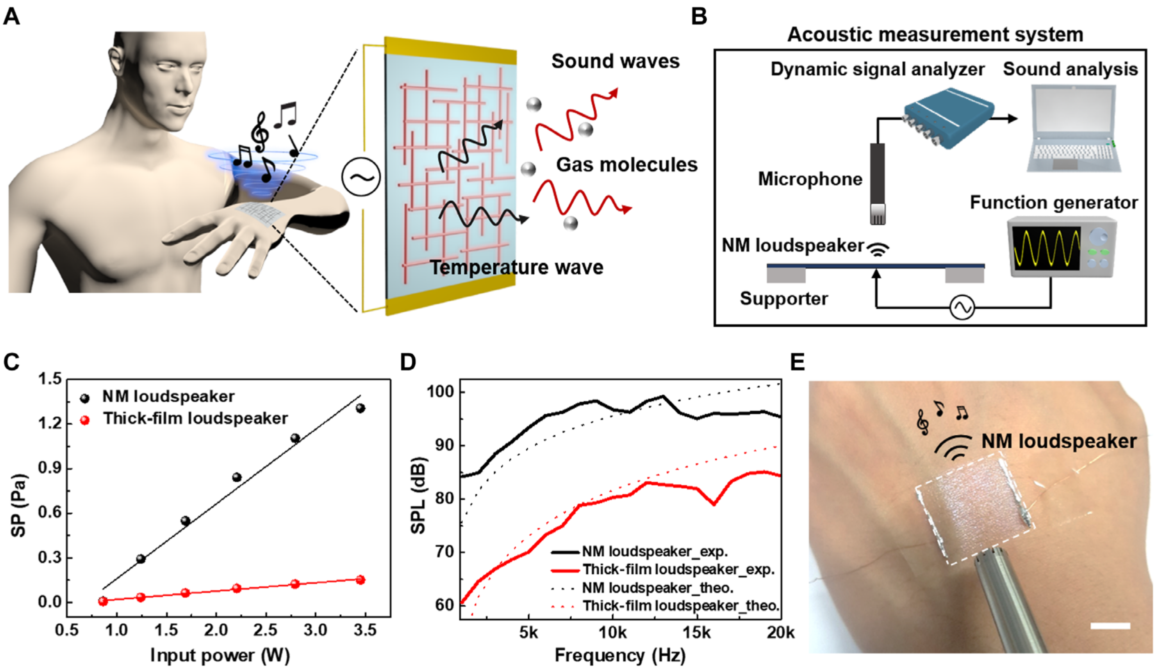

Fig. 4. Skin-attachable NM loudspeaker. (**A**) Schematic of the skin-attachable NM loudspeaker with the orthogonal AgNW array. Sound is generated by temperature oscillation produced by applying an AC voltage. (**B**) Acoustic measurement system where sound emitted from the NM loudspeaker is collected by a commercial microphone with a dynamic signal analyzer. (**C**) Variation in sound pressure (SP) generated from the NM loudspeaker and the thick-film loudspeaker as a function of the input power at 10 kHz. (**D**) Experimental and theoretical values of SPL versus sound frequency for NM and thick PET film loudspeakers. (**E**) Skin-attachable NM loudspeaker mounted on the back of a hand. Scale bar, 1 cm.

micropyramid-patterned PDMS film because it provides the smallest adhesive force with a hybrid NM, in comparison with those of the microdome or micropillar-patterned PDMS films, which can facilitate the contact-separation mode of the NMs (fig. S15). To evaluate the sensitivity of the NM microphone in response to sound emissions, we fabricated two device structures, namely, a freestanding hybrid NM, integrated with a holey PDMS film (NM microphone), and another that was fully adhered to a planar PDMS film without a hole (the thin-film microphone; fig. S16). In addition, we monitored the voltage waveforms emitted by both microphones in response to sound emitted from a speaker, as schematically illustrated in Fig. 5C. Both microphones exhibit narrow and sharp output voltage peaks across a frequency range of 100 Hz to 10 kHz, with the maximum voltage being obtained at 400 Hz, after which it gradually decreases (Fig. 5D). Notably, the NM microphone produces a much higher output voltage than the thin-film microphone across the overall frequency range. Furthermore, we monitored the variations in the output voltage of both microphones with a decreasing SPL at a frequency of 400 Hz to determine their minimum sound-detection capability (Fig. 5E). For the same SPL, the output voltage of the NM microphone was higher than that of the thin-film microphone. These results can be attributed to the excellent vibrational sensitivity of the freestanding NM (*26*), which enhances the coupling of the triboelectric effect with an increase in the gap between the micropyramid-patterned PDMS and the freestanding hybrid NM (*52*). We monitored the time-dependent variation in the voltage waveforms produced by a human voice. A speech entitled "There's plenty of room at the bottom" by R. Feynman was played to both the NM microphone and the thin-film microphone to demonstrate their ability to monitor acoustic waveforms (Fig. 5F). The time-dependent waveform of the output voltage and the corresponding spectrograms obtained from the NM microphone (middle) are in agreement with the original sound waveform and spectrograms (left) of the sentence. On the other hand, the thin-film microphone (right) cannot precisely detect a human voice in that there are some discrepancies in the acoustic waveforms and spectrograms. Moreover, our NM microphone exhibits an excellent acoustic sensing capability, which is comparable to that of a commercial microphone (fig. S17). We also attempted to detect the vibrations produced by the vocal cords while speaking. We observed that an NM microphone attached to a person's neck can clearly detect the phonation of different words (movie S4). This result indicates the applicability of the NM microphone to

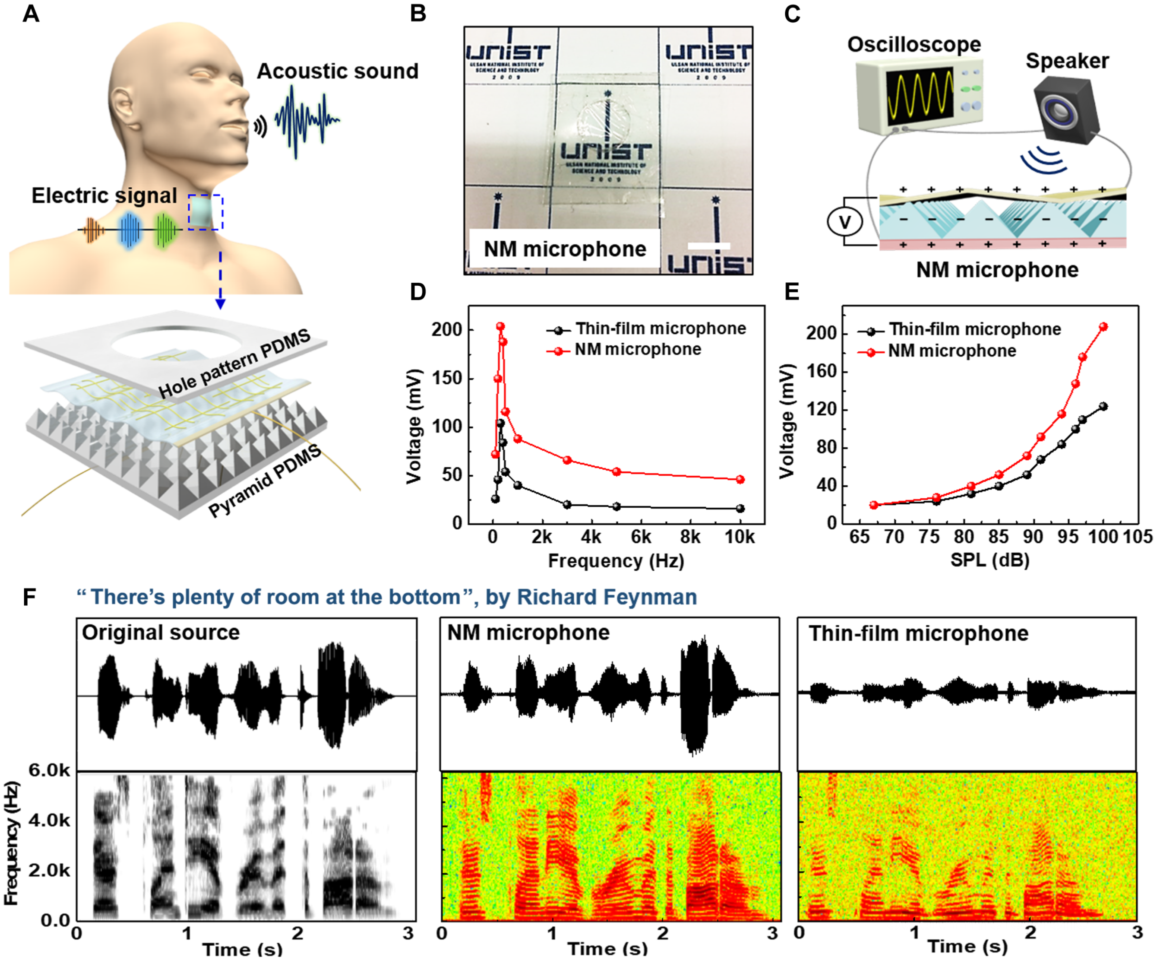

Fig. 5. Wearable and transparent NM microphone. (**A**) Schematic of a wearable NM microphone device. (**B**) Transparent NM microphone placed over the "UNIST" logo, illustrating its transparent and unobtrusive appearance. Scale bar, 1 cm. (**C**) Sensing measurement system for the NM microphone. Variation in the output voltages as a function of (**D**) sound frequency and (**E**) SPL for the NM microphone and the thin-film microphone. (**F**) Waveform and short-time FFT (STFT) signals of original sound ("There's plenty of room at the bottom"; left) extracted by the sound wave analyzer, the signal read from the NM-based microphone (middle), and the thin-film microphone (right).

wearable or skin-attachable electronics, as well as their outstanding acoustic sensing capabilities.

Personal voice security system

As personal information and security became more important, voice recognition has become essential to IoT sensors, voice security, and acoustic interaction with AI. To validate the acoustic sensing capability of the NM microphone and its applicability to human-machine interfaces, we designed a personal voice security system based on the NM microphone, which can recognize a registrant by perceiving the user's voiceprint. Figure 6A shows the voice-based security system with a freestanding NM microphone, which prevents unauthorized users from accessing the system by analyzing the user's voiceprint, as obtained from a recording of the user's voice. In the personal voice security system, we obtained a user's voiceprint using the LabVIEW software, where the sound waveform signal of the user's voice was first recorded by a microphone and then a frequency-domain analysis was performed using FFT with noise filtering. From the FFT spectrum, we arranged the frequency of the user's voiceprint according to the amplitude to quantitatively determine the probability of matching with the frequency ordering of an authorized voiceprint by using customized LabVIEW software (S.C.V Corp.). When the user says "hello" using the NM microphone, the computer analyzes the frequency pattern of the user's voiceprint based on the matching probability, relative to the registered voiceprint (movie S5). If the matching probability is >98%, the computer authorizes the user to access the system, which issues a greeting.

Figure 6B shows the sound waveforms produced in response to the sound of the word "nanomembrane," recorded by a registrant, an authorized user, and a denied user using the NM microphone. The time-dependent acoustic information of the sound waveform of the authorized user corresponds closely to that of the registrant, whereas that of the sound waveform of the denied user is not matched. Figure 6C shows the voiceprints obtained for the original sound waveform produced by the registrant, the authorized user, and the denied user, all of which exhibit a frequency-dependent spectrum. The voiceprints of both the registrant and the authorized user are well matched, with a 99.3% matching probability in the frequency domain. In the analysis of FFTs, they also exhibit similar frequency patterns across the entire range with a higher pitch than that of a denied user (fig. S18). In addition, we could confirm that the overall frequency patterns of FFT obtained from the NM microphone are similar to those obtained with a commercial microphone, although there is a slight discrepancy in the frequency domain of the same voice (fig. S19). To further certify whether the NM microphone could be applied to voice recognition, we compared the matching probabilities obtained using the NM and conventional microphones in response to the voice of a registrant repeating a phrase 10 times (Fig. 6D). Note that the matching probability using the NM microphone exhibited an average reliability of 98.6 ± 0.8% and a small error variance, which is comparable to that

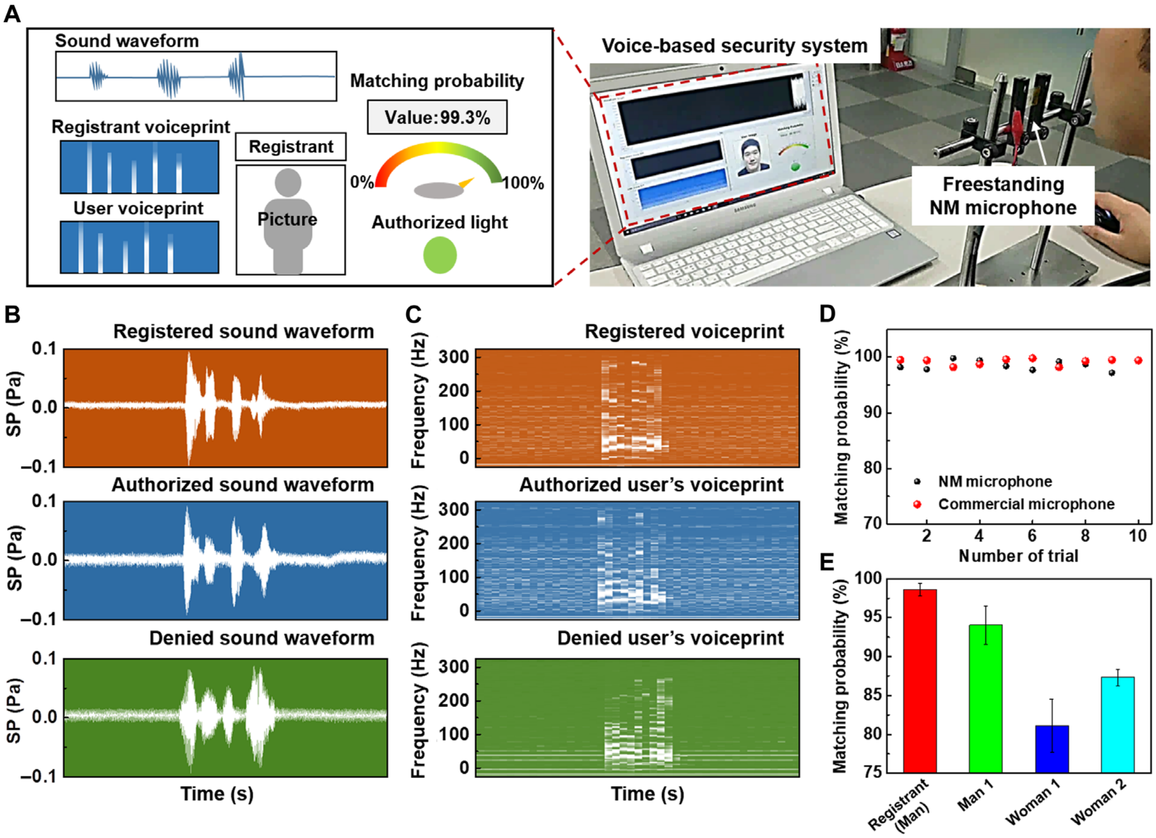

Fig. 6. Personal voice-based security system. (**A**) Schematic of the voice security system (left) and a photograph of the authorization process using the freestanding NM microphone (right). (**B**) Sound waveforms and (**C**) voiceprints collected from the registrant, the authorized user, and the denied user using the NM microphone. (**D**) Matching probability of voiceprint for the authorized user using the NM microphone and a commercial microphone. (**E**) Matching probability of voiceprints obtained from different users including the registrant, a man, and two women. Photo credit: Saewon Kang.

of a commercial microphone (99.1 ± 0.6%), implying that our NM microphone can accurately recognize a registrant's voice with high accuracy and precision. To further validate the precision and selectivity of the NM microphone, we measured the matching probability using the NM microphone in response to voice sounds generated by different persons including the registrant, a man, and two women (Fig. 6E). As a result, our NM microphone can selectively recognize the registrant's voice from different voices, in which all the voice exhibit different and reproducible frequency patterns (fig. S20).

DISCUSSION

In conclusion, we demonstrated a highly conductive and transparent hybrid NM, consisting of an orthogonal AgNW array embedded into a polymer matrix, which provides excellent electrical and mechanical properties compared to pure polymer NMs. Our hybrid NMs facilitate conformal contact with curvilinear and dynamic surfaces without any cracking or rupture. As a conformal/skin-attachable device application, a skin-attachable thermoacoustic NM loudspeaker is presented, enabling intimate contact with human skin and resulting in an imperceptible, transparent appearance. We have also presented a wearable and transparent NM microphone integrated with a micropyramid-patterned PDMS film to precisely detect sounds and vocal vibrations produced by the triboelectric voltage signals corresponding to sounds. As a proof-of-concept demonstration, our NM microphone was applied to a personal voice security system requiring voice-based identification applications. The NM microphone was able to accurately recognize a user's voice and authorize access to the system by the registrant only. These NM-based acoustic devices can be further explored for various potential applications, such as wearable IoT sensors and conformal health care devices.

MATERIALS AND METHODS

Sample preparation

Si substrates were cleaned with isopropyl alcohol and DI water combined with ultrasonication for 5 min each. ZnO films were deposited on Si substrates by a radio frequency sputtering process to act as a sacrificial layer. The ZnO layer was treated with O_2 plasma for 5 min to produce surface wettability and hydrophilicity. Poly-L-lysine (PLL) with amine functional groups was applied to the ZnO films by spin coating at 4000 rpm for 60 s. Orthogonal AgNW arrays were fabricated on the PLL-treated ZnO films by using a modified bar-coating technique in which AgNW ink (Nanopyxis Corp.) containing 0.15 wt % AgNWs in ethanol with an average length of 20 μm and a diameter of 35 nm was used. Parylene-C films were deposited by a CVD method using a parylene coater (Alpha Plus Corp.) on the orthogonal AgNW array to fabricate the hybrid NMs. The as-fabricated hybrid NMs on the ZnO film/Si substrate were placed in an etchant solution (citric acid 10 wt % dispersed in DI water) to remove the ZnO sacrificial layer, which enables the production of freestanding hybrid NMs. The hybrid NM loudspeaker was fabricated by connecting two Cu wires and pasting liquid metal (eutectic gallium-indium) onto the two edges of the hybrid NM. To fabricate a microstructure-patterned PDMS film, we prepared all the PDMS films by mixing a PDMS elastomer base (Sylgard 184, Dow Corning) and a PDMS curing agent (10:1 ratio of base to curing agent). The corresponding mixture of elastomer base and curing agent (liquid PDMS prepolymer) was stored in a vacuum desiccator for 30 min to eliminate the air bubbles. Then, the liquid PDMS prepolymer was poured onto the Si substrate with microstructure patterns (line, pyramid, pillar, and dome) and solidified at 90°C for 3 hours.

Characterization

The surface morphology of the orthogonal AgNW array was examined by an optical microscope (PSM-1000, Olympus). The sheet resistance of the orthogonal AgNW array was measured using a four-point probe method (Keithley 2400). The optical transmittance in the visible range was determined using ultraviolet-visible spectroscopy (JASCO 620). The total thickness of the NMs was measured using atomic force microscopy (DI-3100, Veeco). The applied AC voltage was generated by a function generator (AFG 3011C, Tektronix). The surface temperature of the hybrid NM under the application of AC voltage was monitored by an IR camera (Therm-App TH, Therm-App). A dynamic signal analyzer (National Instruments Corp.), integrated with a commercial microphone (40PH, GRAS), was used to capture the sound emitted by the loudspeaker and analyze the SPL and frequency. The output voltage of the NM microphone was measured using an oscilloscope (DPO 2022B, Tektronix). The adhesion force of micropatterned PDMS films was measured using a texture analyzer (TXA, YEONJIN S-Tech). The voice-based security system was built by using the LabVIEW software with the FFT analysis.

SUPPLEMENTARY MATERIALS

Supplementary material for this article is available at http://advances.sciencemag.org/cgi/content/full/4/8/eaas8772/DC1

Section S1. The calculated bending stiffness of the thin film

Section S2. The measured bending stiffness of the thin film

Fig. S1. Fabrication of the freestanding hybrid NM with the orthogonal AgNW array by removing the sacrificial layer.

Fig. S2. Total thickness of the hybrid NM measured by atomic force microscopy.

Fig. S3. Transmittance in the visible range of 400 to 800 nm and corresponding sheet resistance, R_s, of the orthogonal AgNW array with different numbers of orthogonal coatings.

Fig. S4. The structural design of the hybrid NM for the calculation of the bending stiffness with geometrical parameters illustrated.

Fig. S5. SEM images of the hybrid NM folded in half.

Fig. S6. High-magnitude SEM images of the hybrid NM transferred on the line-patterned PDMS with a line width of 20 μm.

Fig. S7. Estimated step surface coverage of the hybrid NMs with different thickness placed on a micropyramid-patterned PDMS substrate.

Fig. S8. Number of wrinkles generated from a pure parylene NM and hybrid NMs.

Fig. S9. Variation in the number of wrinkles N as a function of $N \sim a^{1/2}h^{-3/4}$.

Fig. S10. Indentation test for measuring the mechanical properties of NMs.

Fig. S11. Loading-unloading indentation test.

Fig. S12. IR images of the orthogonal AgNW array with AC 10 V applied at a frequency of 10 kHz.

Fig. S13. SPL versus distance between the commercial microphone and the thick-film loudspeaker with the orthogonal AgNW array.

Fig. S14. Theoretical values of SPL as a function of sound frequency for loudspeaker with different thickness and substrates.

Fig. S15. Comparison of adhesion force of various micropatterned PDMS films.

Fig. S16. Schematics showing the structure of microphone devices.

Fig. S17. Waveform and STFT signals of original sound ("There's plenty of room at the bottom") extracted by the sound wave analyzer, where the signal was read from a commercial microphone.

Fig. S18. FFTs extracted from the sound wave of the word "nanomembrane" obtained from voices of different subjects including the registrant, the authorized user, and the denied user.

Fig. S19. FFTs extracted from the sound wave, obtained from the voice of a registrant.

Fig. S20. FFTs for a test repeated 10 times, extracted from the sound wave of the word "hello" obtained from various voices of different subjects including the registrant, a man, and two women.

Movie S1. Mechanical durability of hybrid NM.

Movie S2. Compression and stretching test of hybrid NM.

Movie S3. Skin-attachable NM loudspeaker.

Movie S4. The voice recognition using NM microphone.

Movie S5. Voice-based security system.

REFERENCES AND NOTES

1. L. Pan, A. Chortos, G. Yu, Y. Wang, S. Isaacson, R. Allen, Y. Shi, R. Dauskardt, Z. Bao, An ultra-sensitive resistive pressure sensor based on hollow-sphere microstructure induced elasticity in conducting polymer film. *Nat. Commun.* **5**, 3002 (2014).
2. J. Park, M. Kim, Y. Lee, H. S. Lee, H. Ko, Fingertip skin-inspired microstructured ferroelectric skins discriminate static/dynamic pressure and temperature stimuli. *Sci. Adv.* **1**, e1500661 (2015).
3. J. Park, Y. Lee, J. Hong, M. Ha, Y.-D. Jung, H. Lim, S. Y. Kim, H. Ko, Giant tunneling piezoresistance of composite elastomers with interlocked microdome arrays for ultrasensitive and multimodal electronic skins. *ACS Nano* **8**, 4689–4697 (2014).
4. H. S. Lee, J. Chung, G.-T. Hwang, C. K. Jeong, Y. Jung, J.-H. Kwak, H. Kang, M. Byun, W. D. Kim, S. Hur, S.-H. Oh, K. J. Lee, Flexible inorganic piezoelectric acoustic nanosensors for biomimetic artificial hair cells. *Adv. Funct. Mater.* **24**, 6914–6921 (2014).
5. J. Jang, J. Lee, J. H. Jang, H. Choi, A triboelectric-based artificial basilar membrane to mimic cochlear tonotopy. *Adv. Healthc. Mater.* **5**, 2481–2487 (2016).
6. L.-Q. Tao, H. Tian, Y. Liu, Z.-Y. Ju, Y. Pang, Y.-Q. Chen, D.-Y. Wang, X.-G. Tian, J.-C. Yan, N.-Q. Deng, Y. Yang, T.-L. Ren, An intelligent artificial throat with sound-sensing ability based on laser induced graphene. *Nat. Commun.* **8**, 14579 (2017).
7. A. Bertrand, Applications and trends in wireless acoustic sensor networks: A signal processing perspective, in *2011 18th IEEE Symposium on Communications and Vehicular Technology in the Benelux (SCVT)* (IEEE, 2011), pp. 1–6.
8. C. L. Sidner, C. D. Kidd, C. Lee, N. Lesh, Where to look: A study of human-robot engagement, in *Proceedings of the 9th International Conference on Intelligent User Interfaces* (ACM, 2004), pp. 78–84.
9. J. Yang, J. Chen, Y. Liu, W. Yang, Y. Su, Z. L. Wang, Triboelectrification-based organic film nanogenerator for acoustic energy harvesting and self-powered active acoustic sensing. *ACS Nano* **8**, 2649–2657 (2014).
10. X. Fan, J. Chen, J. Yang, P. Bai, Z. Li, Z. L. Wang, Ultrathin, rollable, paper-based triboelectric nanogenerator for acoustic energy harvesting and self-powered sound recording. *ACS Nano* **9**, 4236–4243 (2015).
11. C. Lang, J. Fang, H. Shao, X. Ding, T. Lin, High-sensitivity acoustic sensors from nanofibre webs. *Nat. Commun.* **7**, 11108 (2016).
12. B. Park, J. Kim, D. Kang, C. Jeong, K. S. Kim, J. U. Kim, P. J. Yoo, T.-I. Kim, Dramatically enhanced mechanosensitivity and signal-to-noise ratio of nanoscale crack-based sensors: Effect of crack depth. *Adv. Mater.* **28**, 8130–8137 (2016).
13. O. J. Cheong, J. S. Lee, J. H. Kim, J. Jang, High performance flexible actuator of urchin-like ZnO nanostructure/polyvinylenefluoride hybrid thin film with graphene electrodes for acoustic generator and analyzer. *Small* **12**, 2567–2574 (2016).
14. W. Li, D. Torres, R. Díaz, Z. Wang, C. Wu, C. Wang, Z. L. Wang, N. Sepúlveda, Nanogenerator-based dual-functional and self-powered thin patch loudspeaker or microphone for flexible electronics. *Nat. Commun.* **8**, 15310 (2017).
15. T. Q. Trung, N.-E. Lee, Flexible and stretchable physical sensor integrated platforms for wearable human-activity monitoring and personal healthcare. *Adv. Mater.* **28**, 4338–4372 (2016).
16. M. Kaltenbrunner, T. Sekitani, J. Reeder, T. Yokota, K. Kuribara, T. Tokuhara, M. Drack, R. Schwödiauer, I. Graz, S. Bauer-Gogonea, S. Bauer, T. Someya, An ultra-lightweight design for imperceptible plastic electronics. *Nature* **499**, 458–463 (2013).
17. M. Melzer, M. Kaltenbrunner, D. Makarov, D. Karnaushenko, D. Karnaushenko, T. Sekitani, T. Someya, O. G. Schmidt, Imperceptible magnetoelectronics. *Nat. Commun.* **6**, 6080 (2015).
18. T. Yokota, P. Zalar, M. Kaltenbrunner, H. Jinno, N. Matsuhisa, H. Kitanosako, Y. Tachibana, W. Yukita, M. Koizumi, T. Someya, Ultraflexible organic photonic skin. *Sci. Adv.* **2**, e1501856 (2016).
19. M. S. White, M. Kaltenbrunner, E. D. Glowacki, K. Gutnichenko, G. Kettlgruber, I. Graz, S. Aazou, C. Ulbricht, D. A. M. Egbe, M. C. Miron, Z. Major, M. C. Scharber, T. Sekitani, T. Someya, S. Bauer, N. S. Sariciftci, Ultrathin, highly flexible and stretchable PLEDs. *Nat. Photonics* **7**, 811–816 (2013).
20. D.-H. Kim, J. Viventi, J. J. Amsden, J. Xiao, L. Vigeland, Y.-S. Kim, J. A. Blanco, B. Panilaitis, E. S. Frechette, D. Contreras, D. L. Kaplan, F. G. Omenetto, Y. Huang, K.-C. Hwang, M. R. Zakin, B. Litt, J. A. Rogers, Dissolvable films of silk fibroin for ultrathin conformal bio-integrated electronics. *Nat. Mater.* **9**, 511–517 (2010).
21. M. Park, Y. J. Park, X. Chen, Y.-K. Park, M.-S. Kim, J.-H. Ahn, MoS_2-based tactile sensor for electronic skin applications. *Adv. Mater.* **28**, 2556–2562 (2016).
22. Y. J. Park, S.-K. Lee, M.-S. Kim, H. Kim, J.-H. Ahn, Graphene-based conformal devices. *ACS Nano* **8**, 7655–7662 (2014).
23. A. Miyamoto, S. Lee, N. F. Cooray, S. Lee, M. Mori, N. Matsuhisa, H. Jin, L. Yoda, T. Yokota, A. Itoh, M. Sekino, H. Kawasaki, T. Ebihara, M. Amagai, T. Someya, Inflammation-free, gas-permeable, lightweight, stretchable on-skin electronics with nanomeshes. *Nat. Nanotechnol.* **12**, 907–913 (2017).
24. C. Pang, J. H. Koo, A. Nguyen, J. M. Caves, M.-G. Kim, A. Chortos, K. Kim, P. J. Wang, J. B.-H. Tok, Z. Bao, Highly skin-conformal microhairy sensor for pulse signal amplification. *Adv. Mater.* **27**, 634–640 (2015).
25. M. K. Kwak, H.-E. Jeong, K. Y. Suh, Rational design and enhanced biocompatibility of a dry adhesive medical skin patch. *Adv. Mater.* **23**, 3949–3953 (2011).
26. C. Jiang, S. Markutsya, Y. Pikus, V. V. Tsukruk, Freely suspended nanocomposite membranes as highly sensitive sensors. *Nat. Mater.* **3**, 721–728 (2004).
27. J. A. Rogers, M. G. Lagally, R. G. Nuzzo, Synthesis, assembly and applications of semiconductor nanomembranes. *Nature* **477**, 45–53 (2011).
28. R. Gunawidjaja, C. Jiang, S. Peleshanko, M. Ornatska, S. Singamaneni, V. V. Tsukruk, Flexible and robust 2D arrays of silver nanowires encapsulated within freestanding layer-by-layer films. *Adv. Funct. Mater.* **16**, 2024–2034 (2006).
29. D. D. Kulkarni, I. Choi, S. S. Singamaneni, V. V. Tsukruk, Graphene oxide-polyelectrolyte nanomembranes. *ACS Nano* **4**, 4667–4676 (2010).
30. A. A. Mamedov, N. A. Kotov, M. Prato, D. M. Guldi, J. P. Wicksted, A. Hirsch, Molecular design of strong single-wall carbon nanotube/polyelectrolyte multilayer composites. *Nat. Mater.* **1**, 190–194 (2002).
31. S. Lee, S. Shin, S. Lee, J. Seo, J. Lee, S. Son, H. J. Cho, H. Algadi, S. Al-Sayari, D. E. Kim, T. Lee, Ag nanowire reinforced highly stretchable conductive fibers for wearable electronics. *Adv. Funct. Mater.* **25**, 3114–3121 (2015).
32. C. Mayousse, C. Celle, A. Fraczkiewicz, J.-P. Simonato, Stability of silver nanowire based electrodes under environmental and electrical stresses. *Nanoscale* **7**, 2107–2115 (2015).
33. M. Song, D. S. You, K. Lim, S. Park, S. Jung, C. S. Kim, D.-H. Kim, D.-G. Kim, J.-K. Kim, J. Park, Y.-C. Kang, J. Heo, S.-H. Jin, J. H. Park, J.-W. Kang, Highly efficient and bendable organic solar cells with solution-processed silver nanowire electrodes. *Adv. Funct. Mater.* **23**, 4177–4184 (2013).
34. S. J. Lee, Y.-H. Kim, J. K. Kim, H. Baik, J. H. Park, J. Lee, J. Nam, J. H. Park, T.-W. Lee, G.-R. Yi, J. H. Cho, A roll-to-roll welding process for planarized silver nanowire electrodes. *Nanoscale* **6**, 11828–11834 (2014).
35. J.-Y. Lee, S. T. Connor, Y. Cui, P. Peumans, Solution-processed metal nanowire mesh transparent electrodes. *Nano Lett.* **8**, 689–692 (2008).
36. F. Selzer, N. Weiss, D. Kneppe, L. Bormann, C. Sachse, N. Gaponik, A. Eychmüller, K. Leo, L. Müller-Meskamp, A spray-coating process for highly conductive silver nanowire networks as the transparent top-electrode for small molecule organic photovoltaics. *Nanoscale* **7**, 2777–2783 (2015).
37. R. Gunawidjaja, H. Ko, C. Jiang, V. V. Tsukruk, Buckling behavior of highly oriented silver nanowires eithin layer-by-layer films. *Chem. Mater.* **19**, 2007–2015 (2007).
38. S. Cho, S. Kang, A. Pandya, R. Shanker, Z. Khan, Y. Lee, J. Park, S. L. Craig, H. Ko, Large-area cross-aligned silver nanowire electrodes for flexible, transparent, and force-sensitive mechanochromic touch screens. *ACS Nano* **11**, 4346–4357 (2017).
39. C. Hassler, T. Boretius, T. Stieglitz, Polymers for neural implants. *J. Polym. Sci. Polym. Phys.* **49**, 18–33 (2011).
40. D. Qian, E. C. Dickey, R. Andrews, T. Rantell, Load transfer and deformation mechanisms in carbon nanotube-polystyrene composites. *Appl. Phys. Lett.* **76**, 2868–2870 (2000).
41. P. Podsiadlo, A. K. Kaushik, E. M. Arruda, A. M. Waas, B. S. Shim, J. Xu, H. Nandivada, B. G. Pumplin, J. Lahann, A. Ramamoorthy, N. A. Kotov, Ultrastrong and stiff layered polymer nanocomposites. *Science* **318**, 80–83 (2007).
42. H. Jang, W. Lee, S. M. Won, S. Y. Ryu, D. Lee, J. B. Koo, S.-D. Ahn, C.-W. Yang, M.-H. Jo, J. H. Cho, J. A. Rogers, J.-H. Ahn, Quantum confinement effects in transferrable silicon nanomembranes and their applications on unusual substrates. *Nano Lett.* **13**, 5600–5607 (2013).
43. J. Huang, M. Juszkiewicz, W. H. de Jeu, E. Cerda, T. Emrick, N. Menon, T. P. Russell, Capillary wrinkling of floating thin polymer films. *Science* **317**, 650–653 (2007).
44. D. Kim, S.-H. Kim, J. H. Kim, J.-C. Lee, J.-P. Ahn, S. W. Kim, Failure criterion of silver nanowire electrodes on a polymer substrate for highly flexible devices. *Sci. Rep.* **7**, 45903 (2017).
45. P. Lee, J. Lee, H. Lee, J. Yeo, S. Hong, K. H. Nam, D. Lee, S. S. Lee, S. H. Ko, Highly stretchable and highly conductive metal electrode by very long metal nanowire percolation network. *Adv. Mater.* **24**, 3326–3332 (2012).
46. P. Slobodian, P. Saha, Stress-strain hysteresis of a carbon nanotube network as polymer nanocomposite filler under cyclic deformation. *AIP Conf. Proc.* **1375**, 224–231 (2011).
47. L. Bokobza, Multiwall carbon nanotube elastomeric composites: A review. *Polymer* **48**, 4907–4920 (2007).
48. L. Xiao, Z. Chen, C. Feng, L. Liu, Z.-Q. Bai, Y. Wang, L. Qian, Y. Zhang, Q. Li, K. Jiang, S. Fan, Flexible, stretchable, transparent carbon nanotube thin film loudspeakers. *Nano Lett.* **8**, 4539–4545 (2008).
49. J. W. Suk, K. Kirk, Y. Hao, N. A. Hall, R. S. Ruoff, Thermoacoustic sound generation from monolayer graphene for transparent and flexible sound sources. *Adv. Mater.* **24**, 6342–6347 (2012).
50. C. S. Kim, S. K. Hong, J.-M. Lee, D.-S. Kang, B. J. Cho, J.-W. Choi, Free-standing graphene thermophone on a polymer-mesh substrate. *Small* **12**, 185–189 (2016).
51. L. Lin, Y. Xie, S. Wang, W. Wu, S. Niu, X. Wen, Z. L. Wang, Triboelectric active sensor array for self-powered static and dynamic pressure detection and tactile imaging. *ACS Nano* **7**, 8266–8274 (2013).

52. S. Niu, S. Wang, L. Lin, Y. Liu, Y. S. Zhou, Y. Hu, Z. L. Wang, Theoretical study of contact-mode triboelectric nanogenerators as an effective power source. *Energy Environ. Sci.* **6**, 3576–3583 (2013).

Acknowledgments

Funding: This work was supported by the National Research Foundation of Korea (2015R1A2A1A10054152). **Author contributions:** H.K. conceived the project. S.K. and S.C. performed the entire fabrication process. H.L. and D.-S.U. contributed to the fabrication process. S.K., S.C., R.S., H.L., and J.P. analyzed the resulting data, and all authors provided meaningful feedback for project and manuscript. **Competing interests:** The authors declare that they have no competing interests. **Data and materials availability:** All data needed to evaluate the conclusions in the paper are present in the paper and/or the Supplementary Materials. Additional data related to this paper may be requested from the authors.

Submitted 29 December 2017
Accepted 22 June 2018
Published 3 August 2018
10.1126/sciadv.aas8772

Citation: S. Kang, S. Cho, R. Shanker, H. Lee, J. Park, D.-S. Um, Y. Lee, H. Ko, Transparent and conductive nanomembranes with orthogonal silver nanowire arrays for skin-attachable loudspeakers and microphones. *Sci. Adv.* **4**, eaas8772 (2018).